Thermal inspection for the assessment of adhesively bonded metal adherends

Joseph N. Zalameda[1]*, Peter W. Spaeth[1], Marc Genest[2], Matthew R. Webster[1], and Richard G. Cole[2]

[1]NASA Langley Research Center, Hampton, VA 23681-2199
[2]National Research Council, Ottawa, ON, K1A 0R6, Canada

ABSTRACT

Certification of adhesively bonded structures is currently a challenge for aircraft manufacturers. The ability to certify bonds in primary structure can reduce dependence on fasteners, thus enabling more efficient manufacturing. For example, drilling holes and installing fasteners in bonded joints can be a potentially significant bottleneck in airframe manufacturing. In addition, fasteners increase the airframe weight and can add stress concentration areas. Reducing fastener count can accelerate manufacturing and improve aircraft performance. NASA is currently investigating nondestructive evaluation (NDE) techniques to assess bond integrity. For example, bond thickness influences bond strength, and therefore, NDE techniques are being investigated to determine bond thickness. For bonded metal structures, there is a large difference in the thermal diffusivity between the 7075 aluminum alloy metal adherends and aircraft grade adhesive. Multi-layered thermal models show a large variation in the thermal response for bondline adhesive thicknesses that vary from 100 to 300 microns for adherend thicknesses of 0.163 cm. Experimental through transmission thermal measurements reveal promise to quantitatively characterize the bondline thickness. Results were validated with X-ray computed tomography and optical microscopy measurements, and influence of porosity on the thermal model and measurements are investigated.

Keywords: thermal nondestructive evaluation, thermal diffusivity, bondline thickness, bonded metal adherends, bondline porosity, X-ray computed tomography, optical microscopy

1. INTRODUCTION

The ability to certify bonds in primary load bearing aircraft structures can reduce dependence on fasteners and will enable more efficient manufacturing. For example, drilling holes and installing fasteners in bonded joints can be a potentially significant bottleneck in airframe manufacturing. In addition, fasteners increase the airframe weight and can add stress concentration areas. Reducing fastener count can accelerate manufacturing and improve aircraft performance. NASA is currently investigating nondestructive evaluation (NDE) techniques to assess bond integrity. Studies have shown experimentally that adhesive bondline thickness can significantly affect the strength of the bonded structure [1-3]. In addition, a recently developed phased based ultrasonic method has shown promise for the detection of adhesion between the adherend and adhesive interface by measuring the interfacial stiffness [4-5]. This method also requires measurement of bondline thickness.

Nondestructive techniques such as ultrasound and X-ray computed tomography (CT) are commonly used to measure bondline thickness; however, they have drawbacks. For example, ultrasound requires mechanical contact and a coupling medium to perform the inspection. Recent advances in air coupled and laser ultrasound have shown promise; however, coupling of the energy can still be an issue. Air coupled UT has limited temporal resolution due to the requirement of low frequencies (approximately around a MHz or less) to reduce air impedance mismatches [6]. For laser ultrasound, higher energies can be required to induce thermoelastic heating to produce ultrasonic waves and, therefore, surface ablation can be a potential issue in addition to eye safety precautions [7]. X-ray CT can nondestructively measure bondline thickness;

*joseph.n.zalameda@nasa.gov; phone 1 757-864-4793; fax 1 757-864-4914; http://nde.larc.nasa.gov

however, X-ray CT takes a long time for measurement, has radiation safety precautions, and is only able to inspect small volumes for high resolution measurements.

In this paper we study thermal NDE for the measurement of bondline thickness. The advantages of this NDE technique are it is safe, noncontact and able to inspect large areas rapidly. The application of thermal NDE techniques for the assessment of bond defects has been studied as early as 1985 by Green [8] and others such as Safai and Limerick [9-10]. The thermal NDE setup used is through transmission where the sample is positioned between the heat source and infrared camera. The aluminum samples studied were a bonded single lap joint (SLJ) configuration wherein the aluminum adherend surfaces were grit blasted at certain locations to enhance the surface emissivity and minimize in-plane heat flow. The thermal inspection method is sensitive to the adhesive thickness due to the large difference in the thermal diffusivity between the aluminum adherends and aircraft grade adhesive, and therefore, a thermal inspection technique reveals promise to quantitatively characterize the bondline. Thermal NDE estimation of bondline thickness is validated with X-ray computed tomography and optical microscopy measurements.

2. THERMAL INSPECTION SETUP AND BONDED SAMPLE CONFIGURATION

2.1 Thermal Inspection Setup

The through transmission thermal inspection setup is shown in Figure 1. The thermal inspection system shown has the flash lamps and infrared camera configured on the opposite side with the sample in between. The commercially available inspection system is configured around an infrared camera with a 1344 x 784 indium antimonide (InSb) array operating in the 3 - 5 micron infrared band. The image acquisition data framerate is set to 120 frames per second. A 25 mm focal length germanium lens is used. The camera's noise equivalent temperature difference is less than 0.025 Kelvin. Dual photographic flash lamps powered by two 4800 joule power supplies are placed at the bottom of the inspection system.

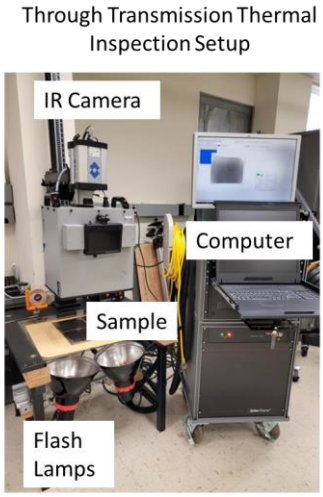

Figure 1: Picture of through transmission thermal inspection system.

2.2 Single Lap Joint Bonded Sample Configuration

The bonded samples were configured for shear mechanical loading. The SLJ samples were bonded using 229 micron diameter wire to control the bondline thickness. The adherends were 1.625 mm thick 7075-T6 aluminum. The adherends were 25.4 mm wide and approximately 101.6 mm long, and were bonded with a 12.7 mm overlap, as shown in Figure 2. Three layers of aircraft grade adhesive film were used during the bonding process. To enhance thermal inspection ability, the samples were grit blasted (220 micron grit) on alternate outer adhered surfaces, as shown in Figure 2. This was necessary to increase the absorption/emissivity on both the surfaces facing the camera and the flash lamps. Grit blasting one side of each adherend forced the conduction of the heat from the bottom adherend (facing the flash lamps) through

the bonded interface toward the top adherend facing the infrared camera, thus minimizing in-plane heat flow. The emissivity of the bare aluminum adherend is measured in comparison to the grit blasted surface as shown in Table 1. Grit blasting the surface enhances emissivity by a factor of over 3, improving the flash lamp energy absorption and the infrared camera's ability to detect the transient thermal response through the bonded region. For comparison, the emissivity of a flat black painted surface is also shown in Table 1. Flat black paint improves the aluminum surface emissivity by a factor of almost 7; however, the thermal diffusivity of flat black paint is typically much lower than the thermal diffusivity of aluminum and closer to the thermal diffusivity of the adhesive. The addition of flat black paint layers would most likely cause errors in the estimate of adhesive thickness. Although grit blasting the aluminum surface slightly alters the adherend thickness, the small changes in thickness were found to be negligible due to the thermal response being dominated by the adhesive thermal properties and thickness.

The SLJ samples were chemically treated to obtain 6 different levels of bond strength using different concentrations of 3-Glycidoxypropyltrimethoxysilane (y-GPS) and Propyltrimethoxysilane (PTMO), as described by Barroeta-Robles [11]. The y-GPS is a reactive agent and the PTMO is a non-reactive agent and therefore is used to chemically degrade the bond. A total of six samples were thermally inspected. These samples concentration levels varied: 100% y-GPS/ 0% PTMO (G100-P0), 70% y-GPS/ 30% PTMO (G70-P30), 50% y-GPS/ 50% PTMO (G50-P50), 30% y-GPS/ 70% PTMO (G30-P70), 25% y-GPS/ 75% PTMO (G25-P75) and 20% y-GPS/ 80% PTMO (G20-P80).

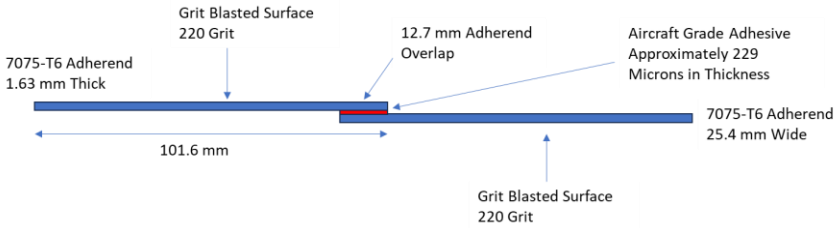

Figure 2: Drawing of SLJ sample configuration.

Table 1: Comparison of Measured Surface Emissivity

Sample	Average Surface Temperature (Celsius)	Measured Emissivity
Unpainted Aluminum Surface	55.6	0.132 +/- 0.0032
Grit Blasted Aluminum Surface	45.7	0.478 +/- 0.0079
Painted Aluminum Surface	34.3	0.90 +/- 0.0080

3. THERMAL MODELING AND MEASUREMENT RESULTS

For bonded metal structures, there is a large difference (factor of over 400) in the thermal diffusivity between the 7075-6 aluminum alloy metal adherends and aircraft grade adhesive. For small adhesive bondline thicknesses as compared to the aluminum adherend thickness, the thermal response will be dominated by the adhesive thermal conductivity and the bondline thickness.

3.1 Thermal Modeling

A three layer one dimensional thermal model is used to estimate the bondline thickness. The layers include the two adherend layers with an adhesive layer in between. The matrix method in the Laplace domain, given by equation (1), is used to solve for the thermal response, assuming perfect thermal contact between the layers and no convection losses [12], where V_1 is the front surface temperature facing the camera, V_0 is the back surface temperature facing the flash heat source, F is the input heat flux at the back surface, l_2 and l_1 are the equivalent adherend thicknesses, K is the aluminum thermal

conductivity, $q = \sqrt{s/\alpha}$, where α is the aluminum thermal diffusivity, K_a is the adhesive thermal conductivity, l_a is the adhesive or bondline thickness, $q_a = \sqrt{s/\alpha_a}$, α_a is the adhesive thermal diffusivity, F is the input heat flux, and s is the Laplace transform parameter.

$$\begin{bmatrix} V_1 \\ 0 \end{bmatrix} = \begin{bmatrix} \cosh(q\ l_2) & \frac{-\sinh(q\ l_2)}{K\ q} \\ -K\ q \sinh(q\ l_2) & \cosh(q\ l_2) \end{bmatrix} \begin{bmatrix} \cosh(q_a l_a) & \frac{-\sinh(q_a l_a)}{K_a\ q_a} \\ -K_a\ q_a \sinh(q_a l_a) & \cosh(q_a l_a) \end{bmatrix} \begin{bmatrix} \cosh(q\ l_1) & \frac{-\sinh(q\ l_1)}{K\ q} \\ -K\ q \sinh(q\ l_1) & \cosh(q\ l_1) \end{bmatrix} \begin{bmatrix} V_0 \\ F \end{bmatrix} \quad (1)$$

Solving equation (1) for V_1 gives the front surface temperature response to estimate the bondline thickness (l_a). This equation is given in (2) as:

$$V_1(s) = \frac{\alpha\ K_a\ F}{\left(\alpha\ K_a \cosh\left[l_2\sqrt{\frac{s}{\alpha}}\right]\left(K\sqrt{\frac{s}{\alpha}}\cosh\left[l_a\sqrt{\frac{s}{\alpha_a}}\right]\sinh\left[l_1\sqrt{\frac{s}{\alpha}}\right]+K_a\sqrt{\frac{s}{\alpha_a}}\cosh\left[l_1\sqrt{\frac{s}{\alpha}}\right]\sinh\left[l_a\sqrt{\frac{s}{\alpha_a}}\right]\right)+ K\sinh\left[l_2\sqrt{\frac{s}{\alpha}}\right]\left(\alpha K_a\sqrt{\frac{s}{\alpha}}\cosh\left[l_1\sqrt{\frac{s}{\alpha}}\right]\cosh\left[l_a\sqrt{\frac{s}{\alpha_a}}\right]+\alpha_a K\sqrt{\frac{s}{\alpha_a}}\sinh\left[l_1\sqrt{\frac{s}{\alpha}}\right]\sinh\left[l_a\sqrt{\frac{s}{\alpha_a}}\right]\right)\right)} \quad (2)$$

Equation (2) was also modified, to take into account porosity in the bondline, where the porosity is modeled as square elements within a medium [13], which in our case is the adhesive. This equation is given in (3) as:

$$K_a = K_{adhesive}\left(1 - \sqrt{\theta}\right) + \frac{K_{adhesive}\sqrt{\theta}}{\left(1 - \sqrt{\theta}\left(1 - \frac{K_{adhesive}}{K_{pore}}\right)\right)} \quad (3)$$

where $K_{adhesive}$ is the thermal conductivity of the adhesive, θ is the volume fraction of the air filled pores, and K_{pore} is the thermal conductivity of air. The values used for this model are presented in Table 2 and the input heat flux, F, is estimated to be 1.71 calorie/sec cm^2 [14]. Using these values, a series of temperature time curves were calculated by varying the adhesive thickness, l_a, from 0 to 1,000 microns in increments of 2 microns then numerically inverting equations (2) and (3) to the time domain [15]. These time domain curves were normalized to the maximum temperature and stored for least squares error minimization to the measured time temperature curves for the estimation of bondline thickness. Example time temperature curves are shown in Figure 3 for adhesive thickness values of 0, 100, 200, and 300 microns. As shown in Figure 3, for 0 micron thickness the temperature reaches a maximum well within 0.2 seconds, for 100 micron adhesive thickness the maximum temperature is reached in approximately 1.5 seconds, for 200 micron adhesive thickness the

Table 2: Model Variable Values at Room Temperature

Input Values	Value	Notes
7075-T6 Aluminum Thermal Diffusivity, α	0.50 cm^2/sec	Laboratory Measured [16]
7075-T6 Aluminum Thermal Conductivity, K	0.32 calorie/^{o}C cm sec	Calculated from Measured Diffusivity, α, using Density and Specific Heat from [17]
Cured Adhesive Thermal Diffusivity, α_a	0.0011 cm^2/sec	Estimated from In-house Modeling Efforts Compared to Experiments
Cured Adhesive Thermal Conductivity, K_a	0.000426 calorie/ ^{o}C cm sec	Calculated from Diffusivity, α_a, using Density and Specific Heat from In-house Modeling Efforts
Air Thermal Conductivity, K_{pore}	0.000061 calorie/ ^{o}C cm sec	From [18]

maximum temperature is reached in approximately 3 seconds, and for 300 micron adhesive thickness the maximum temperature is reached in approximately 4.5 seconds. These results show that for small changes in adhesive thickness a large variation in the thermal response is achieved.

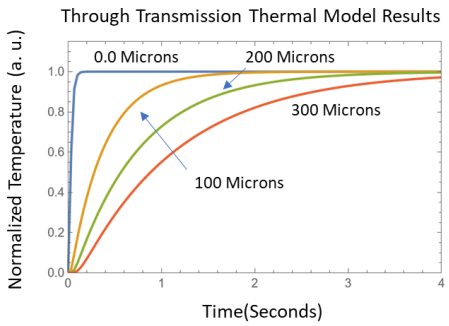

Figure 3: Thermal model response for adhesive thicknesses of 0, 100, 200 and 300 microns.

3.2 Thermal Measurements

Through transmission thermal measurements were performed on six bonded SLJ samples. The samples were configured side by side with the top surface facing the infrared camera as shown in Figure 4(a). Shown in Figure 4(b) is the measurement setup with the flash lamp light shield which prevents heating of the top adherend. Even though the back side of the top adherend was not grit blasted, the measured emissivity of 0.132 would allow some heating; therefore, a flash lamp light shield was utilized. This ensured that the bottom adherend would only be heated and therefore in-plane heat flow would be minimized. The light shield is required for the lap joint configuration, however for flat bonded plates this would not be necessary.

The infrared camera's frame rate was set to 120 Hz and total number of acquired images were 1200 frames for a total inspection time of 10 seconds. For processing, the acquired frames were then boxcar averaged with a window of 4 frames, thus providing an effective frame rate of 30 Hz and a background camera frame, before the flash, was subtracted from the subsequent frames. A single pixel point temperature versus time response is plotted, Figure 5, along with a curve fit using equation (2). Both the model output and measured temperature were normalized to the maximum temperature within the time window of the curve fit (0.367 to 8.33 seconds). The start time of 0.367 seconds was necessary to remove the residual interaction between the infrared camera and the flash lamps after firing and the late time of 8.33 seconds allowed capture of 90% of the maximum steady state temperature. This time window was sufficient to capture the transient rise which is of interest. The series of normalized temperature time curves, produced by varying the adhesive thickness from 0 to 1,000 microns, were compared to the measured data pixel by pixel by minimizing the mean squared difference error to measure bondline thickness for a given porosity level. For this single pixel point case, in Figure 5, the measured bondline thickness

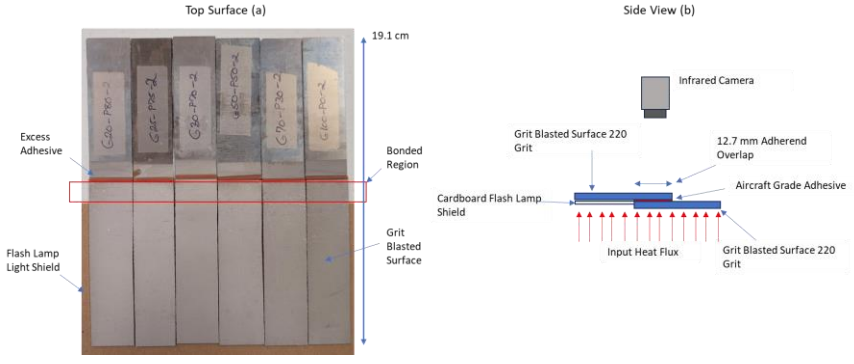

Figure 4: Picture of sample layout for thermal inspection (a) and a side view drawing (b).

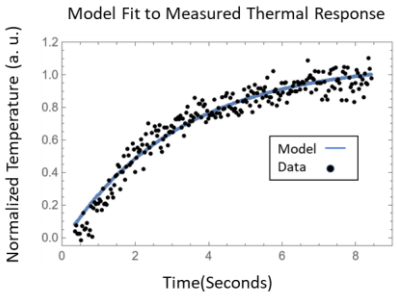

Figure 5: Single pixel plot of measured thermal response and model fit.

was 228 microns for 0% porosity in the adhesive bondline. Shown in Figure 6 are the bonded region thermal inspection images of bondline thickness (0% porosity) for all six samples arranged as shown in Figure 4(a). The bondline thickness histogram and thermal estimation of bondline thickness images for all six samples are shown in Figure 7. It is evident that the bondline thickness estimates are being affected by other factors as shown in the histograms and the variation in thickness estimation mean and standard deviation as shown in Table 3. Also shown in Table 3, are the thermal estimation of bondline thickness with porosity of 7.5%. The thermal thickness estimation is affected by the presence of porosity. For example, for model porosity $\theta = 0\%$, this can increase the thermally measured thickness estimates. Porosity variation will be addressed in the next section using X-ray computed tomography (CT) measurements which indicated significant porosity in the bondline and the optical microscopy analysis which showed an increasing bondline thickness variation from top to bottom.

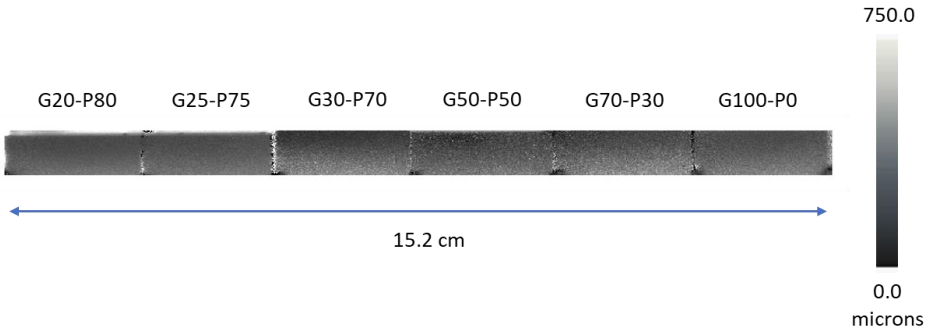

Figure 6: Thermal bondline inspection image for all six SLJ specimens.

4. COMPARISON OF THERMAL MEASUREMENTS TO X-RAY CT

To validate the thermal measurement of effective bondline thickness and to measure porosity, high resolution X-ray CT inspections were performed on all six SLJ specimens. The resolution in the X, Y, and Z directions was 20 microns. The X-ray CT data was obtained by stacking all six specimens and scanning only the bondline region (2.54 cm^3 volume).

4.1 High Resolution X-ray CT Porosity Results

The X-ray CT pore images, in Figure 8 (dark areas are pores), were calculated by averaging 11 planar slices across the bondline. To assist with smoothing the uneven X-ray intensities a nineth order polynomial was fitted in both the X and Y direction for each row or column and then subtracted. The segmentation was performed using a machine learning algorithm trained on multiple X-ray CT data sets [19]. The X-ray CT segmented imagery for porosity volume fraction across the bondline is shown in Figure 8. The segmented porosity or density images range from 0 to 1. For areas of high porosity, the density values would be less (dark areas) as compared to low porosity. The porosity was random and a result of bonding under low vacuum conditions.

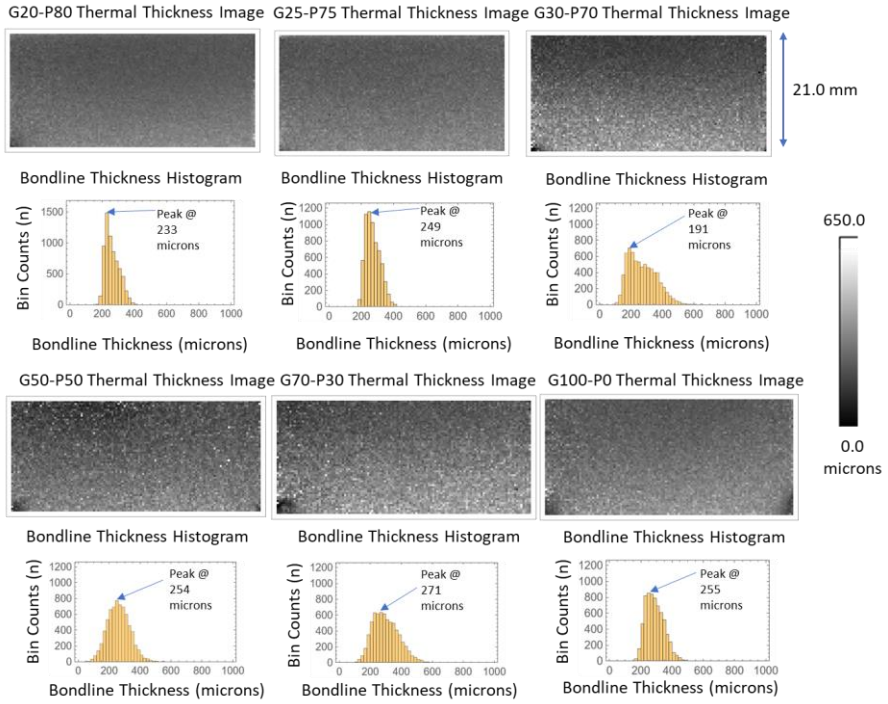

Figure 7: Thermal effective thickness images with respective histograms of bondline thickness.

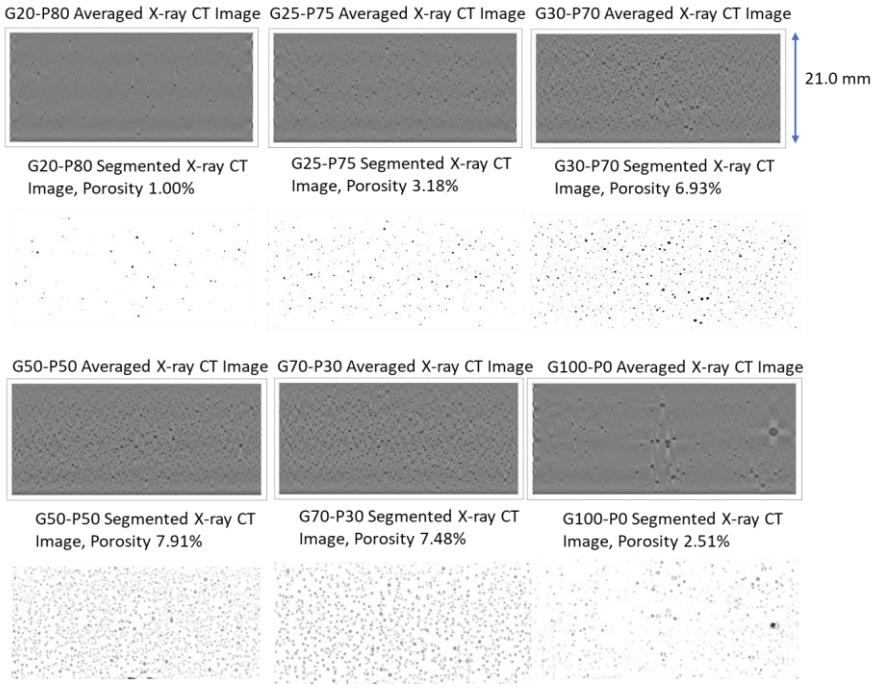

Figure 8: X-ray CT results for porosity volume fraction in the adhesive bondline.

4.2 High Resolution X-ray CT and Optical Microscopy Bondline Thickness Results

The X-ray CT data was analyzed for bondline thickness like the technique used to segment the porosity using the machine learning algorithm [19]. The method differentiates between the metal adherend, porosity, and adhesive. Bondline thickness was estimated from X-ray computed tomography (CT) data using a multi-step image processing approach. Following segmentation of the CT volume, as described previously, the segmented bondline was eroded by two voxels using binary erosion to remove boundary effects, and a thickness map was generated in which each pixel's grayscale value represents the local bondline thickness in voxels. This thickness map was then smoothed using a positive-masked Gaussian filter with a radius of 50 pixels (1.0 mm window), which computes a normalized weighted Gaussian average using only strictly positive pixels in each local neighborhood, thereby preventing background or void regions from biasing the filtered result. The filtered thickness map was subsequently scaled by a factor of 19.9 µm/voxel to convert the voxel-based thickness values to physical units, matching the image pixel resolution of 19.9 µm. The resulting image provides a spatially smooth estimate of bondline thickness, suitable for quantitative analysis. An example image is shown in Figure 9 for the G20-P80 sample. The mode 1, value determined from the histogram, is 230.4 microns and the variance is to within half a voxel. The X-ray CT bondline thickness measurements are compared to the thermal bondline thickness estimates in Table 3. The plot in Figure 10 compares the thermal and X-ray CT estimation of bondline thickness to the X-ray CT measured porosity. Overall, the thermal estimation of bondline thickness appears consistently higher, when the thermal model is not corrected for porosity as compared to the X-ray CT mean bondline thickness measurements. This appears to indicate that the thermal conductivity material property value of the adhesive is high. For higher porosity levels, the thermal bondline

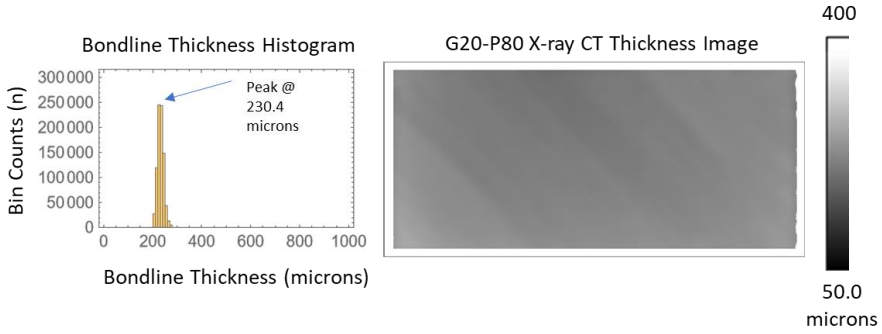

Figure 9: X-ray CT result example for the adhesive bondline thickness imaging for the G20-P80 sample.

Table 3: Comparison of X-ray CT to Thermal NDE for Bondline Thickness Estimates.

Sample	X-ray CT Thickness Mode 1 Histogram Value (microns)	X-ray CT Thickness Mean and Standard Deviation (microns)	X-ray CT Volume Porosity (percent)	Thermal Thickness Mode 1 Histogram Value (microns) $\theta = 0\%$ Porosity	Thermal Thickness Mean and Standard Deviation (microns) $\theta = 0\%$ Porosity	Thermal Thickness Mode 1 Histogram Value (microns) $\theta = 7.5\%$ Porosity	Thermal Thickness Mean and Standard Deviation (microns) $\theta = 7.5\%$ Porosity
G100-P0	246.7	239.5 +/-15.6	2.51	265.4	288.8+/-58.6	213.4	246.0+/-52.6
G70-P30	240.0	231.5 +/-10.5	7.48	273.3	299.7 +/-84.4	215.8	256.6 +/-76.7
G50-P50	239.2	237.4 +/-28.4	7.91	251.2	260.2 +/-72.5	210.2	221.5 +/-64.9
G30-P70	244.1	242.8 +/-13.1	6.93	191.3	271.4 +/-89.4	151.5	231.6 +/-80.1
G25-P75	241.6	245.5 +/-12.2	3.18	241.8	271.6 +/-44.7	208.7	230.4 +/-39.5
G20-P80	230.4	231.5 +/-14.1	1.00	234.9	261.0 +/-43.5	194.5	221.3+/-38.3

thickness measurements are affected by porosity, which explains the wider bondline thickness standard deviations as shown in the Figure 10 plot. When correcting for porosity, (θ = 7.5%) in the thermal model, the thermal estimation measurements compared to the X-ray CT are improved slightly as shown in Table 3 and the plot in Figure 10 when comparing the image mean values.

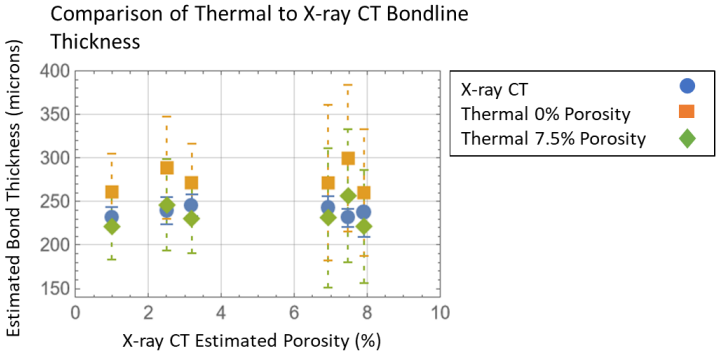

Figure 10: X-ray CT bondline thickness estimation compared to thermal measurements as a function of X-ray CT measured porosity.

High resolution optical microscopy side view images were obtained for all the samples, and an example image is shown in Figure 11 for the G20-P80 sample. For a known pixel resolution, the bondline thickness was determined. Shown in Figure 11 is a plot of the subtle change in increasing bondline thickness from right (approximately 200 microns) to left (approximately 240 microns) with a mean of 218.3 +/- 13.7 microns. This change (evident in all the samples) is most likely due to excess adhesive that has been compressed out unevenly during cure since the edge dam was used on the thicker side. It appears that the X-ray CT image reveals the subtle change in bondline thickness from top to bottom, whereas the thermal imagery clearly shows the increasing thickness from top to bottom as shown in Figure 7.

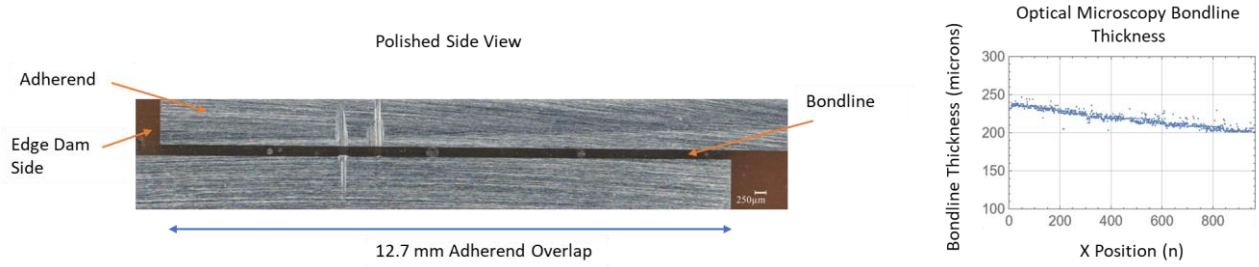

Figure 11: Optical microscopy image showing bondline thickness for the G20-P80 sample.

5. CONCLUSIONS

We demonstrated a thermal inspection technique for the estimation of bondline thickness in bonded metal adherends. Thermal inspection was greatly enhanced by grit blasting the surface. The wide variation in the thermal bondline thickness measurement is due to porosity in the bondline as confirmed with X-ray CT measurements. For porosity greater than 6 percent the thermally estimated bondline thickness error values were significant. The wide variation in the thermally measured bondline thickness can be used as an indication of significant porosity as shown in the thermally measured thickness histograms in Figure 7. Adjusting the porosity within the thermal model provided slightly improved agreement to the X-ray CT bondline thickness measurements as shown in Table 3 and the Figure 11 plot. Spatially registering the X-ray CT measurement of porosity to the thermal measurements would provide a methodology to more accurately thermally estimate effective bondline thickness. If the porosity level is low then the thermal measurement technique can potentially be an effective way to nondestructively estimate effective bondline thickness, especially since the thermal measurement can estimate the bondline thickness over a very large surface area given the thermal inspection is an imaging technique. For a voxel resolution of approximately 19.9 microns, it was necessary to scan over a 2.54 cm^3 volume thus limiting X-

ray CT to small coupons; however, the X-ray CT can separate between the porosity and bondline thickness. Lastly, the thermal inspection was able to show the slightly increasing bondline thickness from top to bottom even for significant porosity levels as shown in Figure 7 and validated with the optical microscopy result in Figure 11.

ACKNOWLEDGEMENTS

The authors would like to thank William Sommers of the Nondestructive Evaluation Sciences Branch for X-ray CT and Brandon Widener for optical microscopy measurements and to thank the Transformational Tools and Technologies Project of the NASA Transformative Aeronautics Concepts Program for research support. Additionally, thanks to Richard Desnoyers, Sandra Robertson and Derek Winfield of NRC for SLJ sample fabrication.

REFERENCES

[1] Kin Loch, A. J. and Shaw, S. J. (1981). The Fracture Resistance of a Toughened Epoxy Adhesive. *The Journal of Adhesion*, *12*(1), 59–77. The Fracture Resistance of a Toughened Epoxy Adhesive: The Journal of Adhesion: Vol 12, No 1

[2] Davies, P., Sohier, L., Cognard, J.Y., Bourmaud, A., Choqueuse, D., Rinnert, E., Creac, R., Influence of adhesive bondline thickness on joint strength, International Journal of Adhesion and Adhesives, 29 (2009), pp. 724-736

[3] Marzi, S., Biel, A., Stigh, U., On experimental methods to investigate the effect of layer thickness on the fracture behavior of adhesively bonded joints, International Journal of Adhesion and Adhesives, 31 (2011), pp. 840-850

[4] Cantrell J, "Assessment of adhesive bond strength from ultrasonic tone bursts," J. Nondestr. Eval. 37, 81 (2018)

[5] Haldren HA, Perey DF, Yost WT, Cramer KE, Gupta MC. Swept-frequency ultrasonic phase evaluation of adhesive bonding in tri-layer structures. J. Acoustic Soc Am. 2019 Mar;145(3):1609. doi: 10.1121/1.5094764. PMID: 31067958; PMCID: PMC7566782.

[6] Frequency considerations in air-coupled ultrasonic inspection. J. Buckley, H. Loertscher. BINDT Conference, Sept. 1999.

[7] Drain, L. E., *Laser Ultrasonics Techniques and Application*, Routledge, New York, 1990.

[8] Green, D. R., "Determining bonding, thickness, and density via thermal wave impedance NDE", 1985, Nasa NTRS#19890004284, Determining bonding, thickness, and density via thermal wave impedance NDE - NASA Technical Reports Server (NTRS)

[9] Safai, M., "Thermography evaluation of metal bonding materials", Proc. SPIE 1682, Thermosense XIV: An Intl Conf on Thermal Sensing and Imaging Diagnostic Applications, (1 April 1992); https://doi.org/10.1117/12.58540

[10] Limerick, R. L., Mtenga, P. V., and Tawfiq, K. S., "IRT Evaluation of Bond Layer Thickness for CFRP Bonded to Concrete", NDT.net Issue: 2004-11, 16th World Conference on NDT - 2004 - Montreal (Canada) (WCNDT 2004).

[11] Robles, J. B., Cole, R., Sands, J.M., and Parker, T., "A Novel Approach to Generation of Adhesive Bonds with Controlled Bond Strength," Proceedings of the American Society for Composites: Twenty-Fifth Technical Conference, Dayton, OH, September 20-22, 2010.

[12] Carslaw, H. S. and Jaeger, J. C., *Conduction of Heat in Solids*, Clarenon Press, Oxford 1986.

[13] Springer, G. and Tsai, W., *Journal of Composite Materials*, Vol. 1, 1967, pp. 166-173.

[14] Winfree, W. P., Cramer, K. E., Zalameda, J. N., Howell, P. A., and Burke, E. R. "Principal component analysis of thermographic data", Proc. SPIE 9485, Thermosense: Thermal Infrared Applications XXXVII, 94850S (12 May 2015); https://doi.org/10.1117/12.2176285

[15] Talbot, A., *IMA J Appl Math* **23 (1)**: 97-120, (1979)

[16] Winfree W. P. and Heath D. M., "Thermal diffusivity imaging of aerospace materials and structures," Proceedings of SPIE, Thermosense, XXIII 3361, pp. 282–290 (1998).

[17] MatWeb Material Property Data, Aluminum 7075-T6, Aluminum 7075-T6; 7075-T651 , Accessed March 10, 2026.

[18] Engineering Toolbox, Air Thermal Conductivity Calculator at 72 Fahrenheit, Air Properties - Thermal Conductivity vs. Temperature and Pressure Charts and Calculator, Accessed March 11, 2026.

[19] Miner, J., Spaeth, P., Frankforter, E., Reyes D., Schneck, W., and Sneha, P., "Impact of Image Noise on Pore Measurement Variability in X-ray Computed Tomography of Additively Manufactured Parts", to be published (2026).